Journal of Colloid and Interface Science 608 (2022) 984–994

Contents lists available at ScienceDirect

Journal of Colloid and Interface Science

journal homepage: www.elsevier.com/locate/jcis

Large-scale synthesis of few-layered copper antimony sulfide nanosheets as electrode materials for high-rate potassium-ion storage

Che-Bin Chang [1], Kuan-Ting Chen [1], Hsing-Yu Tuan *

Department of Chemical Engineering, National Tsing Hua University, Hsinchu 30013, Taiwan

HIGHLIGHTS

- Few-layered $CuSbS_2$ nanosheets were synthesized in gram-scale production.
- Thin 2D layered structure promotes rapid K^+ diffusion kinetics.
- $CuSbS_2$ nanosheets half-cell delivered specific capacities of 177 mAh g^{-1} at 10 A g^{-1}.
- nanosheets PIHC device owing maximum energy density of 127 W h kg^{-1}.

GRAPHICAL ABSTRACT

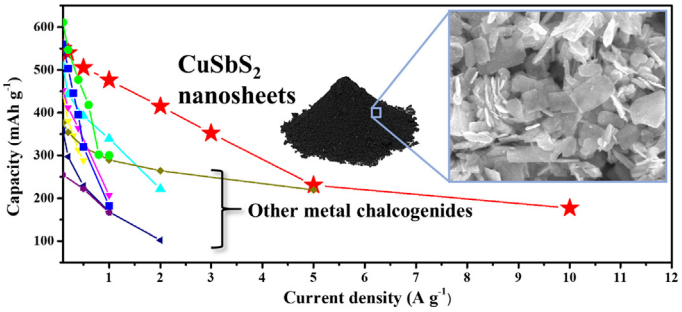

ARTICLE INFO

Article history:
Received 2 August 2021
Revised 23 September 2021
Accepted 24 September 2021
Available online 27 September 2021

Keywords:
Potassium ion storage
Hybrid capacitors
High-rate
Metal chalcogenides
Nanosheets

ABSTRACT

Metal chalcogenides (MCs) have received widespread attentions in potassium ion storage, due to their high theoretical specific capacity and low cost. However, practical applications are still a challenge because of the slow diffusion rate and large ionic radius, leading to dramatic volume expansion and slow rate performance. Herein, we introduce a simple and large scale solvothermal method to synthesize high-quality two-dimensional (2D) layered $CuSbS_2$ nanosheets with a thickness of about 5 nm. The thin 2D layered structure has a weak van der Waals gap and a large exposed surface area to contact the electrolyte and promotes rapid K^+ diffusion kinetics. In addition, the in-situ copper exsolution during potassiation process enhances the rate capability of K^+ storage. $CuSbS_2$ half cells exhibited excellent rate performance, delivering specific capacities of 573, 505, 476, 230, 177 mAh g^{-1} at current densities of 0.1, 0.5, 1, 5, 10 A g^{-1}, respectively. The unique K^+ electrochemical storage mechanism and resistance change during reaction process was revealed in detail by operando XRD, XPS and TEM. Finally, potassium ion hybrid capacitors (PIHCs) with $CuSbS_2$ nanosheets as anode and AC as cathode demonstrated excellent performances with the maximum energy density of 127 W h kg^{-1} and the power density of 2415 W kg^{-1}, providing an example of rationally design a high rate battery-type PIHC anode.

Contents

* Corresponding author.
E-mail address: hytuan@che.nthu.edu.tw (H.-Y. Tuan).
[1] These authors contributed equally to this work.

https://doi.org/10.1016/j.jcis.2021.09.154
0021-9797/

1. Introduction

With the development of portable devices and electric vehicle (EV), energy storage technology has become more and more important [1–3]. Lithium-ion hybrid capacitors (LIHCs) combine the advantages of battery behavior (high energy density) and electrochemical capacitor behavior (high power density and long cycle life) and have become a widely used energy storage system. However, the shortage of lithium metal and uneven distribution in the crust lead to increased costs, making its widespread use in next generation vehicles and devices doubtful [4–6]. Therefore, hybrid capacitors (HCs) with cheap and earth abundant elements (e.g., K, Na, Zn, etc.) were attractive and potential candidates to replace LIHCs. Among them, K has high crust abundance (2.47%) and second-lowest redox potential (−2.93 V) among all the alkali metal, which can provide PIHCs high working potentials and low cost [7–9]. The architecture of PIHCs is composed of battery type anode and capacitor type cathode. Commercial AC has shown well performance in capacitor type cathode; however, battery type anode materials are suffered from sluggish kinetics and large ion radius, causing poor rate performance and the dramatic volume expansion during potassiation/depotassiation [10–14].

Recently, metal chalcogenides (MCs) with layered or non-layered structures, including metal sulfides, metal selenides, or metal telluride, show a great potential as advanced anode materials for K^+ storage due to their low cost, unique electrochemical properties, earth abundance, and high theoretical specific capacity. The M−X bond between MCs is weaker than the M−O bond, which leads to a kinetically more favorable bond cleavage for conversion reaction rather than an intercalation reaction [15]. In addition, the final conversion products of chalcogenides such as M_2S, M_2Se are more conductive than M_2O, providing better reaction kinetic for the ion storage process [16]. However, in the potassium-sulfur or potassium metal sulfide batteries, the severe irreversible side reaction formed by soluble short chain polysulfide will not only lead to poor Columbic efficiency, low rate capability and rapid loss of specific capacity lost, but also infinite recharge [17]. So far, a wide range of binary MCs have been reported, such as MoS_2, $MoSe_2$, WS_2, WSe_2, $FeSe_2$, TiS_2, $NbSe_2$, VS_2, VSe_2, Sb_2S_3, Bi_2S_3, Sb_2Se_3, [18–21] but only a few have studied on ternary MCs. In binary MCs, if the metal element is a transition element, only the chalcogenide can react with K^+, hindering the maximum capacity. If the metal element can react with K^+, e.g., Sb_2S_3, the huge volume expansion will cause the capacity loss greatly.

Ternary MCs can achieve improved electrochemical performance because of the multi-atom synergistic effect induced by additional metal element. Ternary MCs exists in different morphologies, such as particles, rod, nanowires, and nanosheets. Among them, the two-dimensional (2D) structure of nanosheets has received great attention in potassium-ion batteries (PIBs). These 2D materials exhibited unique chemical and physic properties that are different from those of bulk counterparts. Ultra-thin layered 2D materials have a large surface area, which increase the contact area with the electrolyte, and shortens the diffusion distance of metal ions. $CuSbS_2$ (chalcostibite), a ternary layered MCs composed of earth abundant and non-toxic elements: comprise of Sb linked to form SbS_2 chains and, CuS_3 chains by tetrahedra CuS_3. These two types of chains interconnected to form sheets strucuture perpendicular to c-axis [22]. The weak van der Waals force between each layer was different from other transition metal dichalcohenides (TMDs). The atom distribution on surface of $CuSbS_2$ is uneven that affects the Li^+, Na^+, K^+ absorption [23].

Herein, we report the large production of ultra-thin (5 nm) $CuSbS_2$ nanosheets with a high yield (86%) through a simple solvothermal method, using antimony chloride (III) and copper chloride (II) as metal precursor, sulfur-oleylamine solution as surfactant and sulfur source. Because the 2D structure of the thin layer of $CuSbS_2$ exposes a large K^+ diffusion reactive surface area and better adhesion to the conductive agent reduced graphene oxide (rGO), which achieved fast K^+ kinetics. Moreover, the K^+ storage mechanism of $CuSbS_2$ was also revealed by in-situ X-ray diffraction (XRD), ex-situ X-ray photoelectron spectroscopy (XPS) and ex-situ transmission electron microscopy (TEM). The total resistance variety of electrode was analyzed by in-situ electrochemical impedance spectroscopy (EIS). We found that copper was exsolution during the potassiation process at the atomic scale and recombined with sulfur and potassium during the depotassiation process. Benefiting from these advantages, $CuSbS_2$ electrode can deliver high specific capacity of 573 mAh g^{-1} at current density of 100 mA g^{-1}, and even at a high current density of 10000 mA g^{-1}, it still reaches 177 mAh g^{-1}. Moreover, PIHC with $CuSbS_2$ as the anode and activated carbon (AC) as the cathode can provide a maximum energy density of 127 W h Kg^{-1} and a good capacity retention after 1000 cycles.

2. Experimental section

2.1. Materials

Antimony chloride ($SbCl_3$,≧99.95%), ethanol (ACS reagent grade,≧99.5%), copper chloride dihydrate ($CuCl_2{\cdot}2H_2O$, ACS reagent grade,≧99%), copper(II) acetylacetonate ($Cu(C_5H_7O_2)_2$, ≥99.9% trace metals basis), copper (powder, <425 μm, 99.5% trace metals basis), antimony (powder, 100 mesh, 99.5% trace metals basis), sulfur (powder, 99.98% trace metals basis), oleyamine (OLA, technical grade, 70%), toluene (ACS reagent, ≥99.5%), sodium carboxymethyl cellulose (NaCMC, average Mw ~ 700,000), poly(acrylic acid) (PAA, Mv ~ 3,000,000), dimethyl ether (DME, ≧99.8%), 1-Methyl-2-pyrrolidinone (NMP, anhydrous, 99.5%) and potassium metal (chunks in mineral oil, 98%) were purchased from Sigma-Aldrich. Active carbon was purchased from Kuraray Chemical Company.

Potassium bis (fluorosulfonyl) imide (KFSI, 97%) was purchased from Combi-Blocks. Super-P, polyvinylidene fluoride (PVDF) and coin-type cell CR2032 were purchased from shining energy. Glass fiber was purchased from Advantec. Copper and aluminium foil were purchased from Chang-Chun group.

2.2. Synthesis of thin $CuSbS_2$ nanosheets

Typically, 0.6408 g sulfur was added in 120 ml oleyamine via ultrasonic treatment until completely dissolved. Following, 1.36 g copper chloride dihydrate and 1.824 g antimony chloride were added in 40 ml ethanol and continuously stirred to get a clearly green solution. Mixed both solutions and stirred for 5 min, the solution was transferred to 200 ml Teflon-liner. The mixture represented 80% of the reactor volume and sealed by stainless steel autoclave. The autoclave was put in air circulating oven and heated up to 160 °C for 24 h. After solventhermal treatment, the autoclave was cooled to room temperature by natural air cooling. After cooling to room temperature, the $CuSbS_2$ nanosheets were collected and purified by centrifugation with toluene and ethanol (1:1 vol %) for three times, then dried in the vacuum, stored in the argon-filled glove box for the further used.

2.3. Synthesis of thick $CuSbS_2$ nanosheets

First, 1 mmol $Cu(acac)_2$, 1 mmol $SbCl_3$, stir bar and 20 ml OLA were placed into 50 ml three neck round flask, connected with Schlenk line system and purged with argon gas at room temperature for 1 h under stirring. Next, 2.5 mmol sulfur powder was put in 5 ml OLA and treated with ultrasonic until completely dissolved. Then ramp the temperature to 230 °C at the rate of 2 °C min^{-1}. Upon reaching 230 °C, the sulfur-oleyamine solution was quickly inject into metal precursor, the color will change to black immediately, and held at 230 °C for another 1 h with continuous stirring. After reaction, cooling to room temperature, collected the product by centrifugation with toluene and ethanol and dry in vacuum for further use.

2.4. Synthesis of bulk $CuSbS_2$

Bulk $CuSbS_2$ was prepared by mixing 99.99% purity Copper, antimony, sulfur powder stoichiometrically (about 250 mg in total) and sealed in vacuum quartz tube. The quartz tube was put into a muffle furnace which ramped to 800 °C for 24 h with the rate of 1 °C/min avoided to sulfur violent vaporization. After cooling to room temperature, the gray $CuSbS_2$ ingot was obtained.

2.5. Electrochemical measurement

The anode electrode was prepared by mixing active material ($CuSbS_2$ and rGO with the ratio of 6:1), super P, NaCMC, PAA in the ratio of 7:2:0.5:0.5 in distilled water to form a homogeneous slurry. The slurry was coated on the copper foil by doctor blade and dried at 150 °C under argon atmosphere. For the fabrication of cathode electrode for potassium ion hybrid capacitor, active carbon, super P and polyvinyldifluoride (PVDF) were mixed in N-methyl-2-pyrrolidone (NMP) at the ratio of 8:1:1 and then, coating the slurry on aluminum foil dried at 150 °C under argon atmosphere. The mass loading of anode and cathode were roughly $1 \sim 1.2$ mg cm^{-2}, $1.8 \sim 2.5$ mg cm^{-2} respectively. The mass loading of electrode was measured by microbalance with 0.1 μg resolution (Sartorius SE2). The cyclic voltammetry (CV) was collected by multi-channel electrochemical analyzer (Bio-Logic-science Instruments, VMP3). The specific capacity calculation of $CuSbS_2$ electrode is based on total mass of rGO and $CuSbS_2$. The coin-type half-cell (CR2032) was assembled in an argon filled glovebox using home-made K metal foil as a counter electrode. The electrolyte composed of 4 M KFSI in DME was added to infiltrate the anode electrode and glass fiber separator was added, followed by the K foil. After crimping, the battery was taken out from glovebox and tested the electrochemical performance by the Maccor Series 4000 battery test system with the voltage ranging from 0.01 V to 3.0 V. potassium ion hybrid capacitors were assembled with $CuSbS_2$ as the anode, AC as the cathode and 4 M KFSI in DME as the electrolyte, the working window from 0.01 V to 3.8 V. Before potassium ion hybrid capacitors assembling, $CuSbS_2$ anode is pre-potassiation. All the specific capacity calculation for PIHC were based on the active materials both of anode and cathode. The gravimetric energy density (E) and power density (P) were based on the following equation:

$$E = I \int_{t_1}^{t_2} V_t dt / m$$

$$P = \frac{E}{T}$$

In the equation, I (A) is current, V_t (V) is voltage variation with time, m represents the mass (g) of both cathode and anode, T (h) mean the total time of discharge.

3. Result and discussion

The synthesis procedure of $CuSbS_2$ nanosheets is schematically illustrated in Fig. 1a. Briefly, sulfur powder is added to oleylamine, ultrasonically processed to completely dissolve, to prepare an oleylamine-sulfur solution. Then, an ethanol solution containing antimony chloride ($SbCl_3$) and copper chloride dihydrate ($CuCl_2 \cdot 2H_2O$) were added to the oleylamine-sulfur solution to form copper antimony sulfide nanoparticles (Figure S1). Next, the solution was transferred to Teflon-liner and sealed in autoclave for solvothermal reaction and the nanoparticle assembly of $CuSbS_2$ nanosheets was obtained. The scanning electron microscope (SEM) images (Fig. 1b) revealed the high yield of $CuSbS_2$ nanosheets which are uniformly distributed on the substrate. The inset in Fig. 1b is a batch of 1.7 g of $CuSbS_2$ nanosheets with a yield of 86% (1.7 g). The typical $CuSbS_2$ orthorhombic crystal structure was confirmed by XRD (Fig. 1c) with the major diffraction peaks located at 28.4°, 29.9°, 39.1°, 40.2°, 42.6°, 47.9°, 50.3°, 52.0°,respectively indexed to (111), (013), (015), (106), (213), (020), (008) and (122) plane of orthorhombic $CuSbS_2$ with *Pnma* space group and the lattice parameter can be determined to 6.016 Å (a), 3.797 Å (b) and 14.499 Å (c) (JCPDS – 88–0822). The XRD patterns of bulk and thick $CuSbS_2$ nanosheets were shown in Figure S2, and the result is the same as the thin one, but a little impurity in the Sb_2S_3 phase (PDF 00–042-1393). The morphology of $CuSbS_2$ nanosheets prepared by solvothermal method was rectangular, 1–2 μm long, and 200–400 nm wide. It is formed by van der Waals homogeneous epitaxy via the attachment of nanocrystals, restructuring and aggregation of irregular nanocrystals, and eventual forming the rectangular nanosheets structure, only a few layers are stacked and have some irregular nanocrystals attached on the surface. Thick $CuSbS_2$ nanosheets (Figure S3a) were prepared by hot injection method, and were rectangular, with a width of 200–400 nm width, a length of about, and a thickness of 60 nm (Figure S3b). Bulk $CuSbS_2$ has irregular shape and size (Figure S4). Fig. 1f illustrates the crystal structure of the $CuSbS_2$: Cu, Sb, S atoms are covalently boned together by van der Waals forces, and they are stacked in layers that host foreign ions (Li^+, Na^+, K^+) between the layers. [24,25] X-ray photoemission spectroscopy (XPS) spectra were shown in figure g, h, i. In a typical survey spectrum (Figure S5a), the presence of Cu, Sb, S can be confirmed. For further analysis, the high resolution XPS spectra of Cu 2p, Sb 3d,

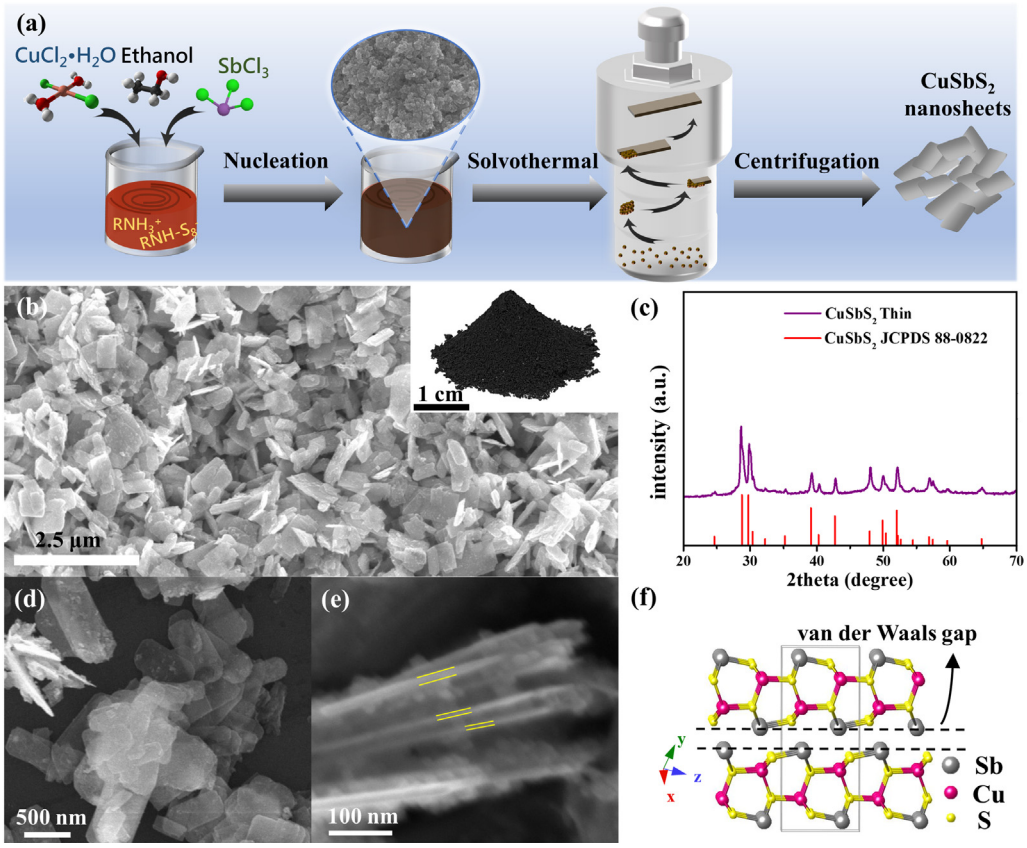

Fig. 1. (a) Schematic illustration of synthesis process of $CuSbS_2$ nanosheet. (b) Low magnification SEM image of $CuSbS_2$ nanosheets (inset photo is $CuSbS_2$ nanosheets synthesized in one batch). (c) XRD pattern of $CuSbS_2$ nanosheets. (d, e) High magnification SEM image of $CuSbS_2$ nanosheets. (f) Crystal structure of $CuSbS_2$.

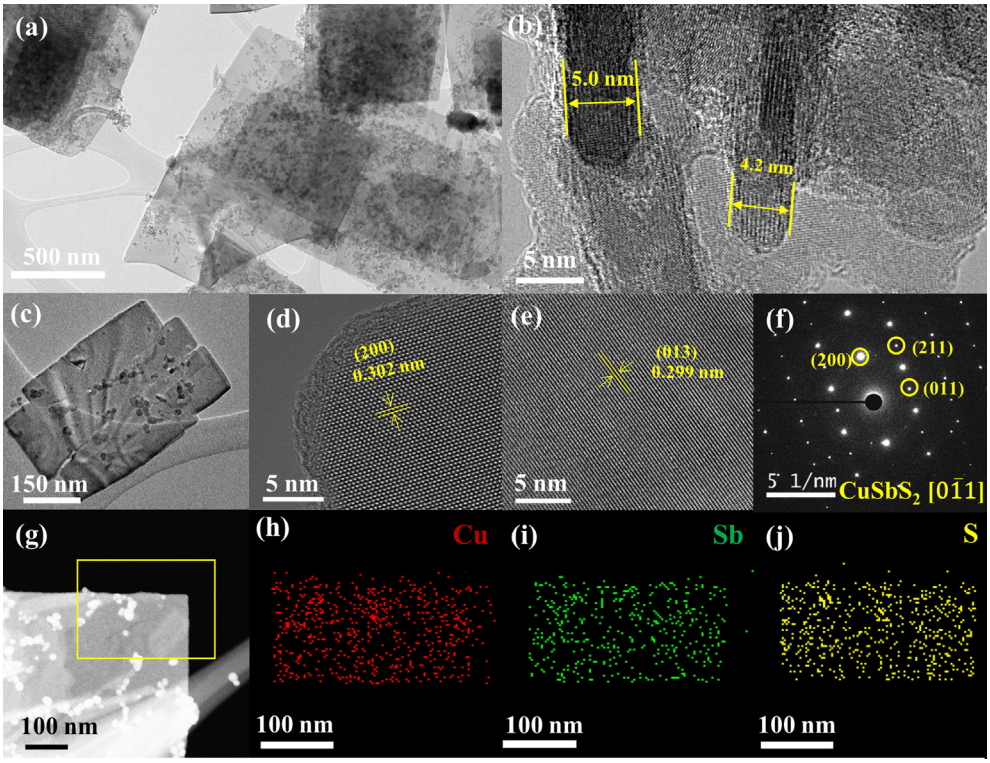

Fig. 2. (a) Low magnification TEM image of $CuSbS_2$ nanosheets. (b) Side view TEM image of $CuSbS_2$ nanosheets. (c) TEM image of single $CuSbS_2$ nanosheets. (d, e) High resolution TEM images of $CuSbS_2$ nanosheets. (f) SAED pattern of $CuSbS_2$ nanosheets. (g) Dark-field TEM image of $CuSbS_2$ nanosheets. EDS mapping a corner of nanosheets for (h) Cu, (i) Sb, (j) S elements.

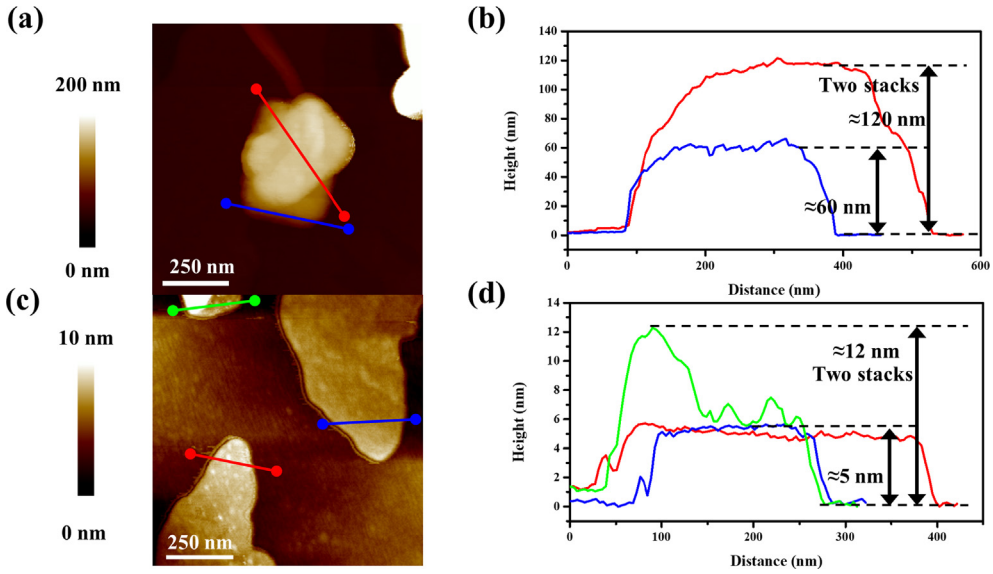

Fig. 3. (a) AFM images of (a) thick, (c) thin $CuSbS_2$ nanosheets. (b, d) Height information of thick and thin $CuSbS_2$ nanosheets.

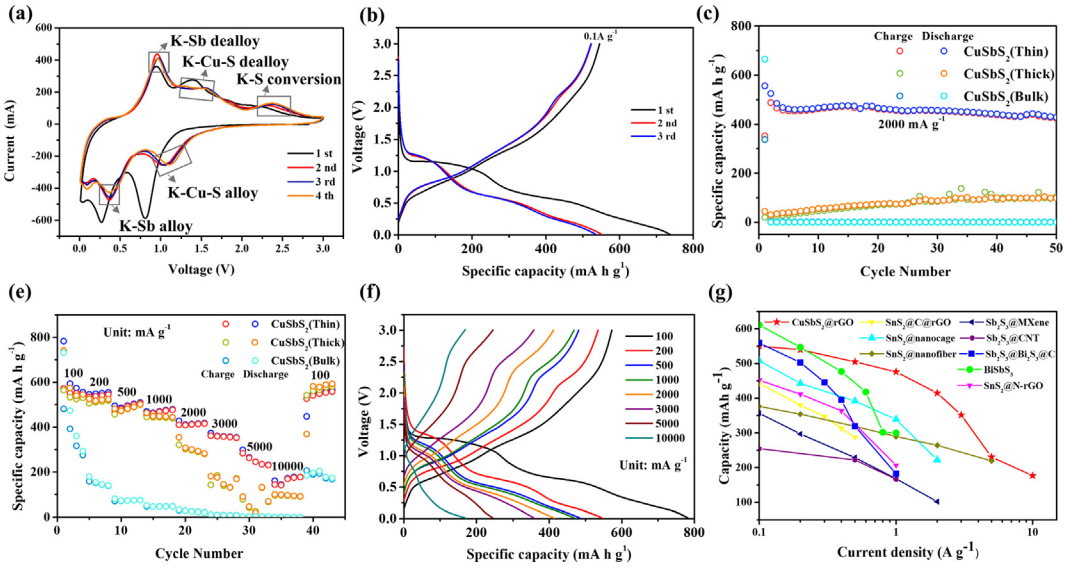

Fig. 4. (a) CV profile of $CuSbS_2$ electrode. (b) Charge/discharge curve of $CuSbS_2$ electrode. (c) Cycling performance of three morphology $CuSbS_2$ electrode. (d) Rate performance of three morphology $CuSbS_2$ electrode. (e) Charge/discharge curve of $CuSbS_2$ at various current density. (f) Comparison of rate capability with others as-reported metal sulfide anode materials.

S 2p was given in Figure S5b-d, respectively. The high resolution of Cu 2p core level spectra shows that there are two major peaks at 932.0 and 950.8 eV, corresponding to Cu $2p_{3/2}$ and Cu $2p_{1/2}$, respectively. In the high resolution XPS spectra of the Sb 3d core level spectrum, an obvious peak can be obtained at 538.6 eV, which is attributed to Sb $3d_{3/2}$ and the peaks at 529.3 eV, which are attributed to Sb $3d_{5/2}$, the slightly shoulder on each peak was attributed to surface oxidation of Sb. The high resolution XPS spectra of the S 2p core energy level shows that the doublet peaks are located at 162.5 and 161.3 eV, which correspond to S $2p_{1/2}$ and S $2p_{3/2}$, respectively.

The low magnification TEM image of the $CuSbS_2$ nanosheets is shown in Fig. 2a. The irregular nanocrystals on the surface can be observed more clearly, confirming the growth mechanism of nanosheets. Fig. 2b shows a side view of $CuSbS_2$ nanosheets, and it can be observed that the thickness is about 5 nm. The TEM image of a single rectangular shape of $CuSbS_2$ nanosheet is shown in Fig. 2c. In the high resolution TEM image (Fig. 2d), a lattice fringe of 0.302 nm corresponds to (200) plane, and another 0.299 nm d-spacing corresponds to (013) plane, which is consistent with the crystal structure of $CuSbS_2$. The selected area electron diffraction pattern (SAED) (Fig. 2f) of the $CuSbS_2$ nanosheets viewed along [022] zone axis shows (200), (211) and (111) lattice diffractions. Additionally, the dark-field TEM images of some nanosheets were shown in Fig. 2g and the elemental mapping of Cu, Sb, S (Fig. 2h-j.) shows the elements Cu, Sb, S distributed evenly in the nanosheets. To further determine the thickness of $CuSbS_2$ nanosheets, we measured it by atomic force microscopy (AFM). Fig. 3a shows the topography of three thin $CuSbS_2$ nanosheets. The height information (Fig. 3b) shows the thin $CuSbS_2$ nanosheets with a thickness about 5 nm and at distance of 100 nm, a height of 12 nm represents two stacks of $CuSbS_2$ nanosheets. In Fig. 3c, two

stacks of thick $CuSbS_2$ nanosheets can be observed. The height information (Fig. 3d) revealed that the thickness of thick $CuSbS_2$ was about 60 nm, which is 12 times thicker than the thin one.

Electrochemical performance of $CuSbS_2$ electrodes were tested with coin cells (CR2032). The specific capacity calculation was based on active materials (both $CuSbS_2$ nanosheets and rGO, Figure S6). Fig. 4a shows a typical cyclic voltammetry (CV) curve of a $CuSbS_2$ electrode at a scan rate of 0.2 mV S^{-1}. In the first cycle, the cathodic peak at 0.75 V was observed and disappeared in the subsequent cycles. This was attributed to the irreversible conversion reaction of $CuSbS_2$ with K^+ and the decomposition of KFSI to form a solid electrolyte interphase (SEI) [26,27]. The second cathodic peak at 0.25 V could be attributed to gradual alloying process of Sb to K_3Sb [9]. In the depotassiation process, there are two obvious anodic peaks at 0.95 V, 1.38 V and the board anodic peak around 2.0 V can be obtained. The two anodic peaks were attributed to the dealloying process of Sb and Cu-K-S, while the board anodic peak was related to S step-conversion process [28]. In the subsequent cycles, the pair of redox peaks at 1.02, 2.37 V were contributed by Cu metal and some potassium polysulfide such as K_2S_4 potassiation/depotassiation process. In addition, another pair of redox peaks at 0.35 and 0.96 V were ascribed to Sb reversible step-alloying/dealloying process [29,30]. Starting from the second cycle, all peaks almost overlap, indicating highly reversible electrochemical performance. Fig. 4b shows the selected galvanostatic charge/discharge curve of $CuSbS_2$ electrode at a current density of 0.1 A g^{-1}, and a working window of 0.01–3.00 V. The initial charge/discharge specific capacities were 736.8 and 551 mAh g^{-1} respectively, representing the initial Coulombic efficiency (ICE) of 74.8%. The irreversible specific capacity loss might be due to SEI layer formation. The first cycling curve shows three discharge/charge plateaus. Expect for the first cycle, the curves overlap, which is consistent with the CV profile. Fig. 4c shows the cycling performance of three different morphologies of $CuSbS_2$ at a current density of 2 A g^{-1}. A fresh battery without K^+ aging have much more resistance than an aging battery, which is more pronounced at high current densities [31]. Among the three types of $CuSbS_2$, only the thin one can overcome the overpotential at a high current density of 2 A g^{-1}, and delivered a specific capacity of 450 mAh g^{-1}. Compared with thick and bulk materials, the thick one only provides specific capacity of 71 mAh g^{-1} and bulk material delivers less than 3 mAh g^{-1}. This result confirms that in the absence of initial activation, the thickness will affect the K^+ storage performance. Also, the electrochemical performance of $CuSbS_2$ electrode in different electrolytes were shown in Figure S7, in 5 M KFSI in EC/DMC The capacity of $CuSbS_2$ electrode remained about 450 mAh g^{-1} at the first 20 cycles, and then immediately decay. In the EC/DEC system, rapid capacity loss was observed in both KPF_6 and KFSI. Therefore, the optimized electrolyte system is 4 M KFSI in DME, which can be cycled over 50 cycles without decay. To further verify the thickness effect at low current density, Fig. 4d shows the rate performance of three type of $CuSbS_2$ at different current densities from 100 mAh g^{-1} to 10000 mA g^{-1}. $CuSbS_2$ electrode exhibited high reversible specific capacities of 550, 540, 505, 476, 415, 352, 230.5, 177 mAh g^{-1} at current densities of 100, 200, 500, 1000, 2000, 3000, 5000, 10000 mA g^{-1}, respectively (Fig. 4e). When the current density returned to 100 mA g^{-1}, the recovered capacity remained at 550 mAh g^{-1} without any capacity loss, showing the excellent rate performance of $CuSbS_2$ electrode. At the low current density of 100 – 1000 mA g^{-1}, thin and thick $CuSbS_2$ nanosheets have not much difference on specific capacity, while the bulk material specific capacity dramatic decrease along with cycling. However, as the current density increased, the difference of specific capacity became larger and larger. At a current density of 2000 mA g^{-1}, the specific capacity of thin $CuSbS_2$ electrode is 130 mAh g^{-1} more than the thick one, and this advantage continues at a higher current density. The excellent rate performance can be attributed to the special van der Waals gap, representing an ideal K^+ diffusion tunnel [32]. In addition, ultra-thin nanosheets provide a larger surface area (17.93 m^2/g) than thick nanosheets (10.44 m^2/g) (Figure S8), which facilitates contact with electrolyte and rGO, thereby shortening the K^+ diffusion distance [33]. On the others hand, Zhang et al. and C. Marino et al. suggested unique in-situ copper exsolution mechanism of $CuSbS_2$ electrode in Li^+, Na^+ storage, which can improve electrode conductivity in atomic scale [26,27]. However, there is a lack of discuss about in-situ copper exsolution in K^+ storage. The comparison of rate capability between our work and previous reports were shown in Fig. 4f. Although the specific capacity of $CuSbS_2$ electrode is lower than $BiSbS_3$ and Sb_2S_3@Bi_2S_3@C in current density of 100, 200 mA g^{-1}, it has the highest reversible specific capacity at higher current densities among all the MCs PIBs anode materials [34–41].

It is well known that sulfide materials exhibit some capacitive behavior in electrochemical process [42]. To understand the kinetic process of the $CuSbS_2$ electrode, different scan rate CV test from 0.1 to 0.9 mV s^{-1} was carried out and shown in Fig. 5a. The response peak currents (i, mA) and scan rate (v, mV s^{-1}) follow the the power law formula below [43]:

$$i = a v^b \tag{1}$$

$$\log i = b \times \log v + \log a \tag{2}$$

Eq. (2) is obtained from the Eq. (1) logarithmically, where a and b are both constants. When the b value is close to 0.5, it means that the reaction is dominated by diffusion control; when the b value is close to 1, represent reaction was pseudocapacitive controlled dominant. Fig. 5b. shows the b value calculated by main cathodic/anodic peak was 0.89, 0.88 for the scan rate of 0.1, 0.3, 0.5, 0.7, 0.9 mV s^{-1}, which revealed that K^+ storage of $CuSbS_2$ electrode was pseudocapacitive controlled. Furthermore, the quantity of pseudocapacitive contribution ratio was calculated by following equation:

$$i = k_1 v^{\frac{1}{2}} + k_2 v \tag{3}$$

$$i/v^{\frac{1}{2}} = k_1 + k_2 v^{\frac{1}{2}} \tag{4}$$

In the equation above, $k_1 v^{\frac{1}{2}}$ indicates diffusion-controlled proportion and $k_2 v$ is pseudocapacitive controlled. The pseudocapacitive contribution ratio of $CuSbS_2$ electrode is calculated to be 90.1% of total (Fig. 5c). The contribution in others scan rate of 0.1, 0.3, 0.5, 0.7 mV s^{-1} were also be calculated to 75.5%, 83.7%, 87.0%, 89.1% respectively (Fig. 5d). High pseudocapacitive contribution ratio may be attributed to ultra-thin 2D structure, which promote the K^+ transport, driving excellent rate performance [44]. To further understand reaction kinetic, galvanostatic intermittent titration technique (GITT) was used. The K^+ diffusion coefficient (D_{k+}) of the $CuSbS_2$ electrode can be estimated by Fick's second law as following [45]:

$$D_{K^+} = \frac{4}{\pi\tau}\left(\frac{V_M m_B}{S M_B}\right)^2 \left(\frac{\Delta E_s}{\Delta E_t}\right)^2 \left(\tau \ll \frac{L^2}{D}\right) \tag{5}$$

Figure S9 show the GITT charge/discharge curve performed at the current density of 200 mA g^{-1} with the 20 min relax time ensure to reached equilibrium state. Before the GITT test, the battery was activated by three cycles. The calculated K^+ diffusion coefficient of $CuSbS_2$ electrode as shown in Fig. 5e was range from 10^{-9} to 10^{-11} cm^2 s^{-1}. Notably, D_{k+} decreasing with the discharge/charge process, which was mainly due to the phase change during potassiation/depotassiation process, corresponding to charge/discharge curve (Figure S9). At the capacity of 66, 200, 400 mAh g^{-1}

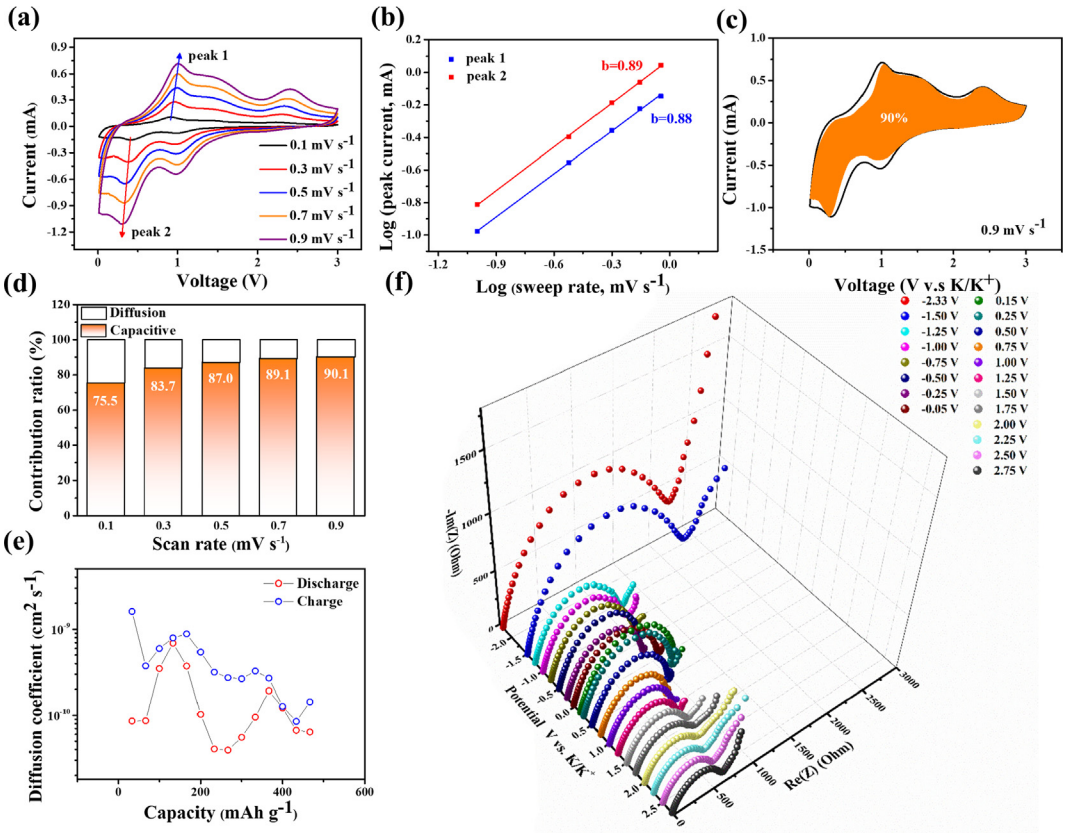

Fig. 5. (a) CV profile of $CuSbS_2$ electrode at various scan rate. (b) Logarithm response current versus logarithm scan rate. (c) Pseudocapacitive contribution at the scan rate of 0.9 mV s^{-1}. (d) The ratio of pseudocapacitive and diffusion contribution at different scan rate. (e) In-situ EIS test performed in selected potentials. (f) Diffusion coefficient distribution along charge/discharge depth.

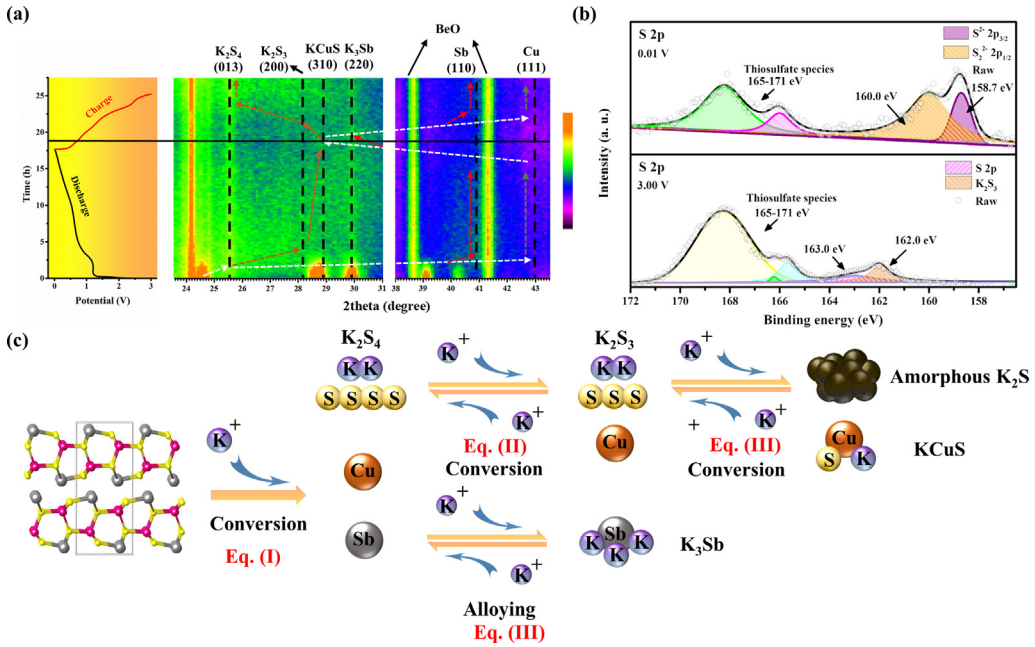

Fig. 6. (a) Contour plot of in-situ XRD information at first charge and discharge process. (b) Ex-situ XPS spectrum of S2p at selected potentials. (c) Schematic illustration of reaction mechanism of $CuSbS_2$.

have three plateau, represent phase changing process, match with the decrease part of D_{k+} [46]. In order to verify copper in-situ exsolution effect on electrode resistance, in-situ EIS also have been conducted. Figure S10 shows the selected potentials from open circuit potential (OCP) 2.30 V discharge to 0.01 V and charge to 3.00 V. The Nyquist plots of selected potentials were shown in Fig. 5f, where

the semi-circle diameter in high frequency region mean K^+ diffusion resistance. In OCP, the $CuSbS_2$ possessed large diffusion resistance, because of the absence of the fast-ion conductor film from fresh electrode [47]. The diffusion resistance decreased slightly with the discharge depth until reaching 0.05 V, resistance slightly increased, due to Cu exsolution and recombination with K, S. In the process of depotassiation, diffusion resistance gradually decreased due to copper exsolution. The Nyquist diagram is fitted with Randles equivalent circuit, where R_{ct}, R_{SEI}, R_e represent charge transfer resistance, SEI layer resistance, electrolytes resistance, respectively. R_{tot} means the sum of R_{ct}, R_{SEI}, R_e in Figure S10b-c, where the increased resistance of 218 Ω at around 0.25 V was obtained, and slightly decreased with charge depth, matching the Nyquist plots (Fig. 4f).

Studies on the reaction mechanism of $CuSbS_2$ in PIBs have not been reported, although there have been some studies in SIBs and LIBs [26,27]. We investigate the phase change mechanism of $CuSbS_2$ electrode using in-situ XRD, ex-situ TEM, and ex-situ SAED to observe the phase transition in the process of potassiation/depotassiation. In Fig. 6a, the left side shows the first discharge and charge curve, and the right side shows the in-situ XRD profile. During the first discharge process to 1.15 V, the $CuSbS_2$ diffraction peaks rapidly weakened and disappeared completely, and did not appear until the end of first plateau, indicating that the $CuSbS_2$ conversion had occurred. Meanwhile, additional peaks appear at 25.5° (013), 28.2° (200), 41° (110) and 43° (111), corresponding to K_2S_4 (PDF 00–030–0992), K_2S_3 (PDF 04–007–0574), Sb (00–005–0562), and Cu (00–004-0836) phase, respectively. When approaching the fully depotassiation state, the characteristic peaks of CuKS (PDF 00–031–0477) and K_3Sb (00–019–0935) at 28.8° (310) and 29.8° (220) gradually increase, which are expressed in the final product; meanwhile, the peaks of Cu and Sb weakened rapidly. During the process of depotassiation, the peaks of Cu and Sb recovered, and the peak intensity of CuKS and K_3Sb gradually weakened. It is worth noting that the theoretical capacity in $CuSbS_2$ was 430 mAh g^{-1} based on the final product of CuKS and K_3Sb, whereas $CuSbS_2$ electrode delivered a reversible capacity of 550 mAh g^{-1} at the current density of 100 mA g^{-1}. We believe that there were some products with low crystallinity, but they are not detected in in-situ XRD. To investigate the final products between the K and S reaction, ex-situ XPS was employed at selected voltages. The high resolution S 2p spectrum is shown in Fig. 6b. When discharged to 0.01 V, the strong peak near 165–171 eV is attributed to the thiosulfate and polythionate species produced by the decomposition of the electrolyte, and the other peaks at 158.7 and 160.0 eV are assigned to S^{2-} (K_2S) and S_2^{2-} (K_2S_2) respectively [48]. The binding energy of K_2S (158.7 eV) and K_2S_2 (160.0 eV) is much lower than that of bulk K_2S (161.2 eV) and K_2S_2 (162.8 eV), which may be caused by the cross-sectional charge transfer effect between rGO and S anion [49]. After reaching the complete

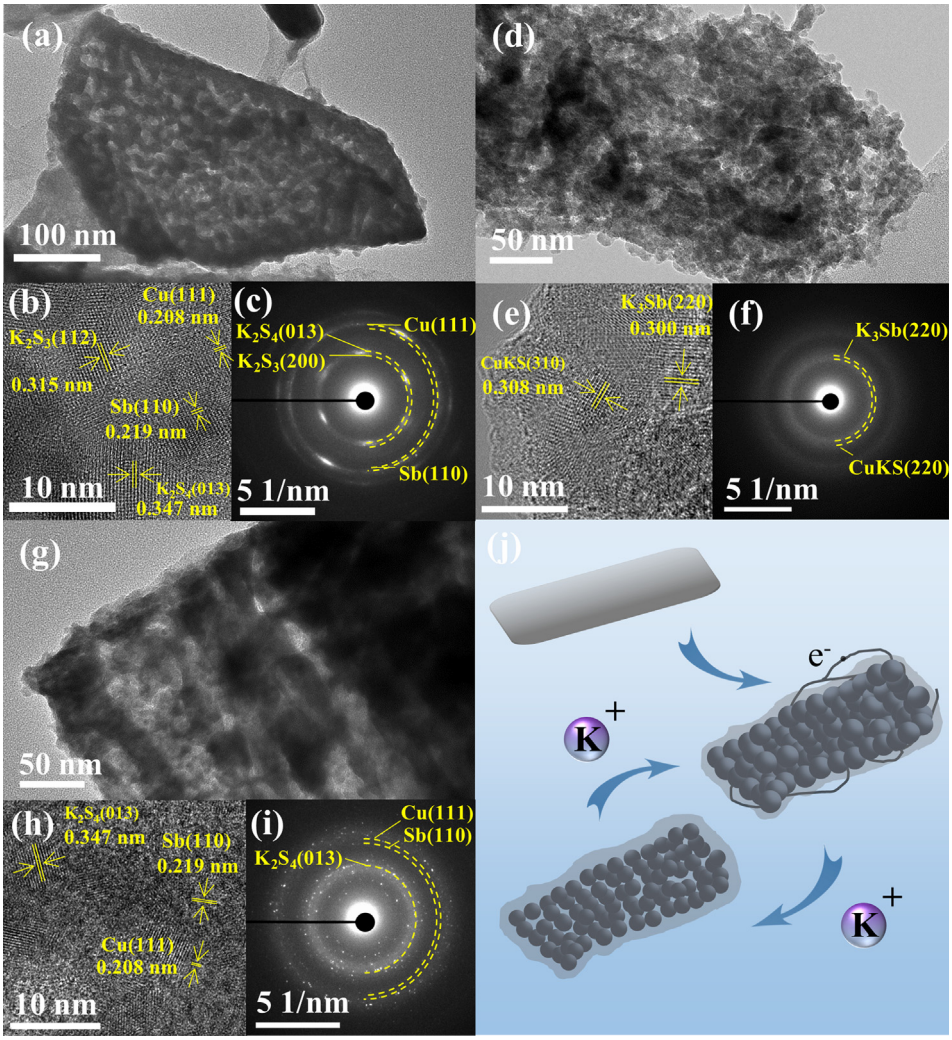

Fig. 7. (a) TEM, (b) HRTEM, (c) SAED pattern of CuSbS2 discharge to 1.15 V. (d) TEM, (e) HRTEM, (f) SAED pattern of $CuSbS_2$ discharge to 0.01 V. (g) TEM, (h) HRTEM, (i) SAED pattern of $CuSbS_2$ charge to 3.00 V. (j) Schematically illustrate morphology evolution of $CuSbS_2$ nanosheets during potassiation/depotassiation process.

depotassiation state, the peaks at 158.7 and 160.0 disappeared and new peaks appeared at 162.0 and 163.0 eV corresponding to K_2S_3 and S, respectively. It indicates the reaction between sulfide and K is highly reversible [50] Based on the above results, we summarize the reaction mechanism in Fig. 6c, which includes irreversible conversion reactions (Eqs. (6) and (7)) and alloy reactions (Eq. (8)). In the reaction, the Eq. (7) reversibility was limited, whereas the Eq. (8) was highly reversible.

$$2CuSbS_2 + 2K^+ + 2e^- \rightarrow K_2S_4 + 2Cu + 2Sb \quad (6)$$

$$3K_2S_4 + 2K^+ + 2e^- \leftrightarrow 4K_2S_3 \quad (7)$$

$$Cu + Sb + K_2S_3 + 6K^+ + 6e^- \leftrightarrow KCuS + K_3Sb + 2K_2S \quad (8)$$

The morphology and intermediated components at the selected potentials were further characterized by ex-situ TEM as shown in Fig. 7. At a potential of 1.15 V (Fig. 7a) (corresponding to $CuSbS_2$ conversion reaction), some nanoparticles appeared on the surface of $CuSbS_2$ and still maintain the shape of nanosheets. In the HRTEM image (Fig. 7b), the lattice fringes of 0.208, 0.219, 0.315, 0.347 nm respectively represent Cu (1 1 1), Sb (1 1 0), K_2S_3 (1 1 2), K_2S_4 (0 1 3), consistent with the information obtained in SAED pattern (Fig. 7c). In Fig. 7d, as the discharge process reaches the fully potassiated state, the morphology of nanosheets changes to nanoparticles aggregation. Notably, the aggregation maintains the shape of sheet, indicating that the sheet structure can buffer the volume expansion and prevent pulverization. The lattice fringes of 0.300 and 0.308 nm (Fig. 7e) are indexed to K_3Sb (2 2 0) and KCuS (3 1 0), respectively, and can be also observed in the SAED pattern (Fig. 7f). When it reaches 3.00 V (Fig. 7g), it represents a complete depotassiation state, and the morphology-maintaining nanoparticles aggregate and maintain keeping the flake shape in a fully potassiated state, indicating a stable potassiation/depotassiation process. Moreover, the lattice fringes of 0.208, 0.219, and 0.347 nm (Fig. 7h) are indexed to Cu (1 1 1), Sb (1 1 0), and K_2S_4 (0 1 3) respectively; corresponding SAED pattern was shown in Fig. 7i. According to ex-situ TEM observation, the nanosheets structure would be converted to nanoparticle aggregation during the potassiation state. While achieving complete depotassiation, the morphology maintains the nanoparticle aggregation, but the nanosheet shape was maintained providing stable K^+ storage process. To better understand stability of $CuSbS_2$ nanosheets, SEM images of three different morphology $CuSbS_2$ electrode after 20 cycles was shown in Figure S11. Figure S11a shows the thin $CuSbS_2$ nanosheets after cycling: the same nanoparticle aggregation in nanosheet shape as TEM images can be obtained, whereas thick $CuSbS_2$ (Figure S11b) can't maintain the nanosheet structure. In Figure S11c, bulk $CuSbS_2$ electrode cracked in many small pieces, leading to rapidly capacity loss.

Based on the previous results, the excellent electrochemical performance of $CuSbS_2$ electrode can be attributed to following advantages: (1) weak van der Waals gaps allow K^+ effectively diffuse into $CuSbS_2$ structure; (2) in-situ copper exsolution can increase the electrode conductivity at the atomic scale, resulting in excellent rate capability; (3) The ultrathin 2D structure of the sheet can buffer large volume expansion and expand the contact area between the electrolyte and the electrode during the potassisation/depotassiation process. Therefore, these merits of fast K^+ kinetic match the battery type anode requirements of PIHC. The PIHC device was assembled with $CuSbS_2$ as anode and AC as cathode with the mass ratio of 1:2.5. The upper CV curve in Fig. 8a

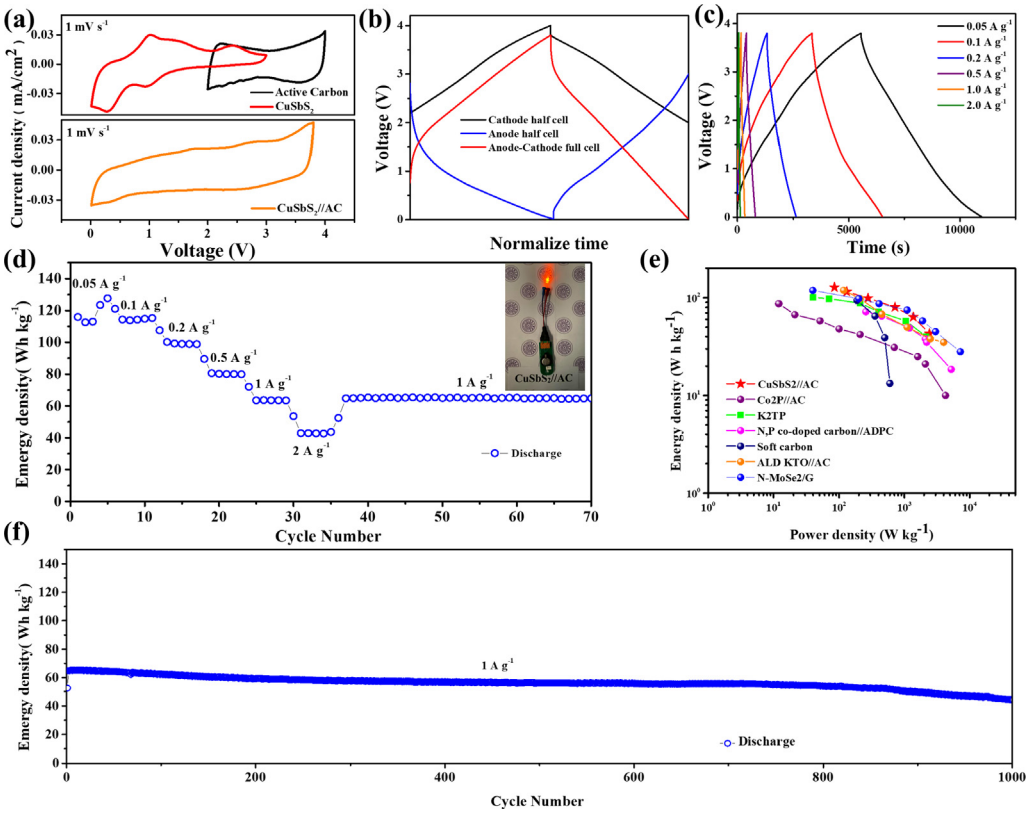

Fig. 8. (a) CV profile of AC and $CuSbS_2$ half cell (top), CV profile of $CuSbS_2$//AC PIHC (bottom). (b) Voltage versus normalize time curve of half and full cells. (c) Charge/discharge curve of $CuSbS_2$//AC at various current density. (d) Rate performance of $CuSbS_2$//AC full cells. (e) Ragone plot of $CuSbS_2$//AC full cells compared with others 2D materials. (f) Cycling performance of $CuSbS_2$//AC full cells.

shows the working window of $CuSbS_2$ and AC. Generally, the working window of a PIHC device depends on the cathode cut-off voltage subtract anode charging curve. Therefore, the working window of $CuSbS_2$ is from 0.01 V to 4.00 V. However, in the range above 3.80 V, the response current peak becomes sharp, due to the decomposition of the electrolyte [51]. Therefore, the optimized working window of PIHC is set from 0.01 to 3.80 V, as shown at the bottom of Fig. 7a. The charge/discharge curves of AC half-cell at 2.00–4.00 V, $CuSbS_2$ half-cell at 0.01–3.00 V, and $CuSbS_2$//AC full cells at 0.01–3.80 V are shown in Fig. 8b. Fig. 8c shows the charge discharge curves of PIHC at different current densities. In addition, the $CuSbS_2$//AC PIHC can deliver an energy density of 127.7 W h kg^{-1} at a current density of 50 mA g^{-1} and operating for about 11000 s. Furthermore, at higher current densities of 100, 200, 500, 1000, 2000 mA g^{-1} high energy densities of 115.3, 99.3, 80.1, 63.5, 42.9 W h kg^{-1} can be obtained, respectively, as shown in Fig. 8d. Besides, PIHC device can easily light LED up. Comparison of energy/power density Ragone plot between $CuSbS_2$ and Co_2P//AC, K_2TP//AC, N, P co-doped carbon//ADPC, soft carbon, ALD KTO//AC, N-$MoSe_2$/G//AC were shown in Fig. 8e. Due to the few-layered nanosheets structure and van der waals gaps, providing expected larger surface area contact with rGO, not only efficiency increase contact area to electrolyte but also shorten the distance of K^+ diffusion. Furthermore, in-situ copper exsolution mechanism allow copper atom exsolution in atomic scale during charge/discharge process, which reduced the resistance of electrode, promote fast ion migration. These advantages make the ternary MCs $CuSbS_2$ display its competitiveness with others PIHC [52–57]. The cycling performance of $CuSbS_2$ is shown in Fig. 8f. At the current density of 1000 mA g^{-1}, it can deliver 64 W h kg^{-1} over 1000 cycles with a retention of 68%. These results show that $CuSbS_2$ as a promising anode material of PIHC with high energy/power density and long cycling life span.

4. Conclusion

In summary, we provide a simple hydrothermal method for large scale synthesis of $CuSbS_2$ nanosheets as an anode material for advanced high performance PIHC. The special van der waals gaps and ultrathin 2D structure not only allow fast K^+ diffusion kinetics, but also improve cycle stability. The unique in-situ copper exsolution reaction mechanism could improve the electrode conductivity and deliver excellent rate capability (177 mAh g^{-1} at current density of 10000 mA g^{-1}). In addition, in-situ XRD, ex-situ XPS, and ex-situ TEM reveal the reaction mechanism of $CuSbS_2$ during the K^+ insertion extraction process. We demonstrate a PIHC with $CuSbS_2$//AC configuration can provide high energy/power density of 127 W h kg^{-1} /2415 W kg^{-1} with long cycle life span of 1000 cycles. This work provides an efficient scalable method to syntheses $CuSbS_2$ nanosheets with excellent K^+ rate capability which might inspire more anode materials with structural uniqueness for high performance K^+ storage.

CRediT authorship contribution statement

Che-Bin Chang: Methodology, Data curation, Investigation. **Kuan-Ting Chen:** Conceptualization, Data curation, Investigation. **Hsing-Yu Tuan:** Supervision, Conceptualization, Writing – review & editing.

Declaration of Competing Interest

The authors declare that they have no known competing financial interests or personal relationships that could have appeared to influence the work reported in this paper.

Acknowledgment

This work was financially supported from the Young Scholar Fellowship Program by Ministry of Science and Technology in Taiwan, under Grant of MOST 108-2636-E-007-013, MOST 108-2622-8-007-016, and MOST 109-2636-E-007-011.We also thank the technical support from Ms. Y. M. Chang in Instrumentation Center at National Tsing Hua University.

Appendix A. Supplementary data

Supporting Information Available. SEM images and XRD pattern of thick, bulk $CuSbS_2$; XPS spectra of $CuSbS_2$; SEM images of $CuSbS_2$ and rGO; electrochemical performance of $CuSbS_2$ electrode in different electrolyte; GITT, in-situ EIS charge/discharge curve of $CuSbS_2$ electrode. Supplementary data to this article can be found online at https://doi.org/10.1016/j.jcis.2021.09.154.

References

[1] F. Cheng, J. Liang, Z. Tao, J. Chen, Functional materials for rechargeable batteries, Adv. Mater. 23 (15) (2011) 1695–1715.
[2] X. Min, J. Xiao, M. Fang, W.A. Wang, Y. Zhao, Y. Liu, A.M. Abdelkader, K. Xi, R.V. Kumar, Z. Huang, Potassium-ion batteries: outlook on present and future technologies, Energy Environ. Sci. 14 (4) (2021) 2186–2243.
[3] P. Poizot, S. Laruelle, S. Grugeon, L. Dupont, J.-M. Tarascon, Nano-sized transition-metal oxides as negative-electrode materials for lithium-ion batteries, Nature 407 (6803) (2000) 496–499.
[4] W. Zhang, J. Mao, S. Li, Z. Chen, Z. Guo, Phosphorus-based alloy materials for advanced potassium-ion battery anode, J. Am. Chem. Soc. 139 (9) (2017) 3316–3319.
[5] A. Eftekhari, Z. Jian, X. Ji, Potassium secondary batteries, ACS Appl. Mater. Interf. 9 (5) (2017) 4404–4419.
[6] W. Wang, J. Zhou, Z. Wang, L. Zhao, P. Li, Y. Yang, C. Yang, H. Huang, S. Guo, Short-range order in mesoporous carbon boosts potassium-ion battery performance, Adv. Energy Mater. 8 (5) (2018) 1701648.
[7] A.P. Cohn, N. Muralidharan, R. Carter, K. Share, L. Oakes, C.L. Pint, Durable potassium ion battery electrodes from high-rate cointercalation into graphitic carbons, J. Mater. Chem. A 4 (39) (2016) 14954–14959.
[8] D. Larcher, J.-M. Tarascon, Towards greener and more sustainable batteries for electrical energy storage, Nature Chem. 7 (1) (2015) 19–29.
[9] J. Zheng, Y. Yang, X. Fan, G. Ji, X. Ji, H. Wang, S. Hou, M.R. Zachariah, C. Wang, Extremely stable antimony–carbon composite anodes for potassium-ion batteries, Energy Environ. Sci. 12 (2) (2019) 615–623.
[10] X. Hu, Y. Liu, J. Chen, L. Yi, H. Zhan, Z. Wen, Fast redox kinetics in bi-heteroatom doped 3D porous carbon nanosheets for high-performance hybrid potassium-ion battery capacitors, Adv. Energy Mater. 9 (42) (2019) 1901533.
[11] D. Qiu, J. Guan, M. Li, C. Kang, J. Wei, Y. Li, Z. Xie, F. Wang, R.u. Yang, Kinetics enhanced nitrogen-doped hierarchical porous hollow carbon spheres boosting advanced potassium-ion hybrid capacitors, Adv. Funct. Mater. 29 (32) (2019) 1903496.
[12] J. Ge, L. Fan, J. Wang, Q. Zhang, Z. Liu, E. Zhang, Q. Liu, X. Yu, B. Lu, $MoSe_2$/N-doped carbon as anodes for potassium-ion batteries, Adv. Energy Mater. 8 (29) (2018) 1801477.
[13] M. Chen, W. Wang, X. Liang, S. Gong, J. Liu, Q. Wang, S. Guo, H. Yang, Sulfur/oxygen codoped porous hard carbon microspheres for high-performance potassium-ion batteries, Adv. Energy Mater. 8 (19) (2018) 1800171.
[14] A. Mohammadi Zardkhoshoui, B. Ameri, S.S. Hosseiny Davarani, A high-energy-density supercapacitor with multi-shelled nickel–manganese selenide hollow spheres as cathode and double-shell nickel–iron selenide hollow spheres as anode electrodes, Nanoscale 13 (5) (2021) 2931–2945.
[15] Q. Zhou, L.i. Liu, Z. Huang, L. Yi, X. Wang, G. Cao, Co_3S_4@ polyaniline nanotubes as high-performance anode materials for sodium ion batteries, J. Mater. Chem. A 4 (15) (2016) 5505–5516.
[16] H. Tan, Y. Feng, X. Rui, Y. Yu, S. Huang, Metal chalcogenides: paving the way for high-performance sodium/potassium-ion batteries, Small Methods 4 (1) (2020) 1900563.
[17] L. Wang, J. Bao, Q. Liu, C.-F. Sun, Concentrated electrolytes unlock the full energy potential of potassium-sulfur battery chemistry, Energy Stor. Mater. 18 (2019) 470–475.
[18] M. Pumera, Z. Sofer, A. Ambrosi, Layered transition metal dichalcogenides for electrochemical energy generation and storage, J. Mater. Chem. A 2 (24) (2014) 8981–8987.
[19] A.M. Zardkhoshoui, B. Ameri, S.S.H. Davarani, α-MnS@Co_3S_4 hollow nanospheres assembled from nanosheets for hybrid supercapacitors, Chem. Eng. J. 422 (2021) 129953.
[20] A.M. Zardkhoshoui, S.S. Hosseiny Davarani, An efficient hybrid supercapacitor based on Zn–Mn–Ni–S@ NiSe core–shell architectures, Sustainable Energy Fuels 5 (3) (2021) 900–913.

[21] A. Mohammadi Zardkhoshoui, S.S. Hosseiny Davarani, M. Maleka Ashtiani, M. Sarparast, Designing an asymmetric device based on graphene wrapped yolk–double shell $NiGa_2S_4$ hollow microspheres and graphene wrapped FeS_2–$FeSe_2$ core–shell cratered spheres with outstanding energy density, J. Mater. Chem. A 7 (17) (2019) 10282–10292.
[22] J.T.R. Dufton, A. Walsh, P.M. Panchmatia, L.M. Peter, D. Colombara, M.S. Islam, Structural and electronic properties of $CuSbS_2$ and $CuBiS_2$: potential absorber materials for thin-film solar cells, Phys. Chem. Chem. Phys. 14 (20) (2012) 7229.
[23] K. Ramasamy, R.K. Gupta, H. Sims, S. Palchoudhury, S. Ivanov, A. Gupta, Layered ternary sulfide $CuSbS_2$ nanoplates for flexible solid-state supercapacitors, J. Mater. Chem. A 3 (25) (2015) 13263–13274.
[24] K. Ramasamy, H. Sims, W.H. Butler, A. Gupta, Mono-, few-, and multiple layers of copper antimony sulfide ($CuSbS_2$): a ternary layered sulfide, J. Am. Chem. Soc. 136 (4) (2014) 1587–1598.
[25] L. Cao, S. Yang, W. Gao, Z. Liu, Y. Gong, L. Ma, G. Shi, S. Lei, Y. Zhang, S. Zhang, R. Vajtai, P.M. Ajayan, Direct laser-patterned micro-supercapacitors from paintable MoS_2 films, Small 9 (17) (2013) 2905–2910.
[26] C. Marino, T. Block, R. Pöttgen, C. Villevieille, $CuSbS_2$ as a negative electrode material for sodium ion batteries, J. Power Sources 342 (2017) 616–622.
[27] Z. Zhang, C. Zhou, Y. Liu, J. Li, Y. Lai, M. Jia, $CuSbS_2$ nanobricks as electrode materials for lithium ion batteries, Int. J. Electrochem. Sci. 8 (10059) (2013) e10067.
[28] J. Li, W. Qin, J. Xie, H. Lei, Y. Zhu, W. Huang, X. Xu, Z. Zhao, W. Mai, Sulphur-doped reduced graphene oxide sponges as high-performance free-standing anodes for K-ion storage, Nano Energy 53 (2018) 415–424.
[29] Y. An, Y. Tian, L. Ci, S. Xiong, J. Feng, Y. Qian, Micron-sized nanoporous antimony with tunable porosity for high-performance potassium-ion batteries, ACS Nano 12 (12) (2018) 12932–12940.
[30] K. Cao, H. Liu, Y. Jia, Z. Zhang, Y. Jiang, X. Liu, K.-J. Huang, L. Jiao, Flexible antimony@ carbon integrated anode for high-performance potassium-ion battery, Adv. Mater. Technol. 5 (6) (2020) 2000199.
[31] S. Yang, G.D. Park, Y.C. Kang, Conversion reaction mechanism of cobalt telluride-carbon composite microspheres synthesized by spray pyrolysis process for K-ion storage, Appl. Surf. Sci. 529 (2020) 147140.
[32] Y. Xu, F. Bahmani, M. Zhou, Y. Li, C. Zhang, F. Liang, S.H. Kazemi, U. Kaiser, G. Meng, Y. Lei, Enhancing potassium-ion battery performance by defect and interlayer engineering, Nanoscale Horiz. 4 (1) (2019) 202–207.
[33] G. Wang, X. Xiong, D. Xie, Z. Lin, J. Zheng, F. Zheng, Y. Li, Y. Liu, C. Yang, M. Liu, Chemically activated hollow carbon nanospheres as a high-performance anode material for potassium ion batteries, J. Mater. Chem. A 6 (47) (2018) 24317–24323.
[34] J. Wang, L. Fan, Z. Liu, S. Chen, Q. Zhang, L. Wang, H. Yang, X. Yu, B. Lu, In situ alloying strategy for exceptional potassium ion batteries, ACS Nano 13 (3) (2019) 3703–3713.
[35] L. Cao, B. Zhang, X. Ou, C. Wang, C. Peng, J. Zhang, Interlayer expanded SnS_2 anchored on nitrogen-doped graphene nanosheets with enhanced potassium storage, Chem. ElectroChem. 6 (8) (2019) 2254–2263.
[36] D. Li, L. Dai, X. Ren, F. Ji, Q. Sun, Y. Zhang, L. Ci, Foldable potassium-ion batteries enabled by free-standing and flexible SnS_2@ C nanofibers, Energy Environ. Sci. 14 (1) (2021) 424–436.
[37] D. Li, Q. Sun, Y. Zhang, L. Chen, Z. Wang, Z. Liang, P. Si, L. Ci, Surface-confined SnS_2@C@ rGO as high-performance anode materials for sodium-and potassium-ion batteries, Chem. Sus. Chem. 12 (12) (2019) 2689–2700.
[38] K. Li, X. Liu, Y. Qin, Z. Zhao, Y. Xu, Y. Yi, H. Guan, Y. Fu, P. Liu, D. Li, Sb_2S_3-Bi_2S_3 microrods with the combined action of carbon encapsulation and rGO confinement for improving high cycle stability in sodium/potassium storage, Chem. Eng. J. 414 (2021) 128787.
[39] M. Li, F. Huang, J. Pan, L. Li, Y. Zhang, Q. Yao, H. Zhou, J. Deng, Amorphous Sb_2S_3 nanospheres in-situ grown on carbon nanotubes: anodes for NIBs and KIBs, Nanomaterials 9 (9) (2019) 1323.
[40] Q. Sun, D. Li, L. Dai, Z. Liang, L. Ci, Structural engineering of SnS_2 encapsulated in carbon nanoboxes for high-performance Sodium/Potassium-ion batteries anodes, Small 16 (45) (2020) 2005023.
[41] T. Wang, D. Shen, H. Liu, H. Chen, Q. Liu, B. Lu, A Sb_2S_3 Nanoflower/MXene Composite as an Anode for Potassium-Ion Batteries, ACS Appl. Mater. Interf. (2020).
[42] X. Jia, E. Zhang, X. Yu, B. Lu, Facile Synthesis of Copper Sulfide Nanosheet@ Graphene Oxide for the Anode of Potassium-Ion Batteries, Energy Technol. 8 (1) (2020) 1900987.
[43] V. Augustyn, J. Come, M.A. Lowe, J.W. Kim, P.-L. Taberna, S.H. Tolbert, H.D. Abruña, P. Simon, B. Dunn, High-rate electrochemical energy storage through Li^+ intercalation pseudocapacitance, Nat. Mater. 12 (6) (2013) 518–522.
[44] B. Luo, P. Wu, J. Zhang, L. Cao, C. Wang, B. Lu, B. Zhang, X. Ou, Van der Waals heterostructure engineering by 2D space-confinement for advanced potassium-ion storage, Nano Res. (2021) 1–10.
[45] Z. Jian, Z. Xing, C. Bommier, Z. Li, X. Ji, Hard carbon microspheres: potassium-ion anode versus sodium-ion anode, Adv. Energy Mater. 6 (3) (2016) 1501874.
[46] X. Li, H. Liang, X. Liu, R. Sun, Z. Qin, H. Fan, Y. Zhang, Ion-exchange strategy of CoS_2/Sb_2S_3 hetero-structured nanocrystals encapsulated into 3D interpenetrating dual-carbon framework for high-performance Na^+/K^+ batteries, Chem. Eng. J. 425 (2021) 130657.
[47] L. Liu, Y.u. Chen, Y. Xie, P. Tao, Z. Wang, Q. Li, K. Wang, C. Yan, Enhanced interfacial kinetics of carbon monolith boosting ultrafast Na-storage, Small 15 (5) (2019) 1804158.
[48] Y. Song, W. Zhao, L. Kong, L.i. Zhang, X. Zhu, Y. Shao, F. Ding, Q. Zhang, J. Sun, Z. Liu, Synchronous immobilization and conversion of polysulfides on a VO_2–VN binary host targeting high sulfur load Li–S batteries, Energy Environ. Sci. 11 (9) (2018) 2620–2630.
[49] P. Xiong, X. Han, X. Zhao, P. Bai, Y. Liu, J. Sun, Y. Xu, Room-temperature potassium–sulfur batteries enabled by microporous carbon stabilized small-molecule sulfur cathodes, ACS Nano 13 (2) (2019) 2536–2543.
[50] X. Zhao, Y. Hong, M. Cheng, S. Wang, L. Zheng, J. Wang, Y. Xu, High performance potassium–sulfur batteries and their reaction mechanism, J. Mater. Chem. A 8 (21) (2020) 10875–10884.
[51] N. Xiao, W.D. McCulloch, Y. Wu, Reversible dendrite-free potassium plating and stripping electrochemistry for potassium secondary batteries, J. Am. Chem. Soc. 139 (28) (2017) 9475–9478.
[52] Y. Wang, Z. Zhang, G. Wang, X. Yang, Y. Sui, F. Du, B.o. Zou, Ultrafine Co_2P nanorods wrapped by graphene enable a long cycle life performance for a hybrid potassium-ion capacitor, Nanoscale Horiz. 4 (6) (2019) 1394–1401.
[53] Y. Yi, Z. Sun, C. Li, Z. Tian, C. Lu, Y. Shao, J. Li, J. Sun, Z. Liu, Designing 3D biomorphic nitrogen-doped $MoSe_2$/graphene composites toward high-performance potassium-ion capacitors, Adv. Funct. Mater. 30 (4) (2020) 1903878.
[54] D. Li, C. Liu, D. Huang, M. Zhang, X. Zhang, H. Gou, F. Yin, G. Wang, Atomic layer deposition regulating hydrated $K_2Ti_6O_{13}$ nanobelts on graphene platform with accelerated solid solution potassiation for potassium ion capacitors, Chem. Eng. J. 417 (2021) 128048.
[55] Y. Luo, L. Liu, K. Lei, J. Shi, G. Xu, F. Li, J. Chen, A nonaqueous potassium-ion hybrid capacitor enabled by two-dimensional diffusion pathways of dipotassium terephthalate, Chem. Sci. 10 (7) (2019) 2048–2052.
[56] X.u. Yu, M. Shao, X. Yang, C. Li, T. Li, D. Li, R. Wang, L. Yin, A high-performance potassium-ion capacitor based on a porous carbon cathode originated from the Aldol reaction product, Chin. Chem. Lett. 31 (9) (2020) 2215–2218.
[57] L. Fan, K. Lin, J. Wang, R. Ma, B. Lu, A nonaqueous potassium–based battery–supercapacitor hybrid device, Adv. Mater. 30 (20) (2018) 1800804.